A new cross-saturated torque model of highly utilized synchronous reluctance machine

COSMAS UCHENNA OGBUKA[1], CAJETHAN NWOSU[2], GIDEON UMOH[3]

Department of Electrical Engineering
University of Nigeria, Nsukka
e-mail: {cosmas.ogbuka / cajethan nwosu}@unn.edu.ng, umohgideon@gmail.com

Abstract: A new cross-saturated torque model of the synchronous reluctance machine (SynRM) including a direct incorporation of cross-saturation effects is presented. Direct-quadrature (d-q axes) flux linkages for both saturation and cross-saturation conditions, obtained experimentally through current decay test using open winding fixed rotor method, are accurately curve-fitted and linearization between the two extremes yielding analytical functions for cross-coupled d-q axes flux linkages. These flux linkages are used to achieve a cross-saturated flux linkage-based torque model for highly utilized SynRM. The accuracy of the developed torque model is evaluated by comparing with the experimentally measured torque of a 5.5 kW SynRM in a dynamometer test bench which also measures and account for the effect of iron losses. The close similarity of the experimental results with the developed model proves the accuracy of the model and its suitability for direct incorporation in control algorithms of advanced SynRM drives without the use of look-up tables.

Key words: synchronous reluctance machine, cross-saturation, direct-quadrature axes, flux linkage

1. Introduction

Recent rotor design enhancements have made the synchronous reluctance machine (SynRM) competitive compared to traditional machines in medium and low power applications [1–3]. The SynRM has theoretically no rotor losses resulting in higher efficiency, torque density and temperature capability than the induction machine (IM). Absence of rotor permanent magnets immunes the SynRM to demagnetization [4] while it maintains the advantage of reduced torque ripple, noise and vibration over the switched reluctance machine (SRM) [5]. Its construction is also simple and rugged [1]. The above qualities make the SynRM a good alternative in a wide variety of industrial applications, even in variable speed operations up to the field weakening region [6–9].

To achieve high torque density, extreme saturation of ferromagnetic parts occurs in highly utilized SynRM resulting in the variation of inductances which determine the electromechanical

torque characteristics [10–11]. Cross-saturation phenomenon arises because the *d-q* axes flux linkages depend on the current in both axes thereby making the flux linkages extremely nonlinear with increases in the axes currents [5, 12–13].

The use of look-up tables and the online parameter estimation methods for the incorporation of cross-saturation were dominate but not without the attendant limitations [14]. Though simple, the look-up table requires large volume of data and memory capacity. Again, the results are not continuous and are confined within a specified measured limit needing interpolation, the accuracy of which depends on the experience of the researcher. The online parameter estimation [15–18] is prone to error resulting in poor dynamic performance. Offline estimation of inductance, using finite element method, is also possible if the exact knowledge of the geometry and material composition of the machine is guaranteed [19–21]. The computational complexity of finite element method makes it not suitable for use in real-time control algorithm.

To overcome the above challenges, this paper presents an accurate torque model of the SynRM explicitly incorporating saturation and cross-saturation effects. The accuracy of the developed model is verified, experimentally, with the performance of a laboratory 5.5 kW SynRM dynamometer test bench which takes account of the inevitable effects of iron losses.

2. A conceptual cross-saturated torque model of the SynRM

Compared to the torque model of the PMSM reported in [22–23], the torque model of the SynRM, due to the absence of magnetic excitation, for an unsaturated machine is:

$$T_e = \frac{3}{2}\frac{P}{2}(L_d - L_q)\,i_d i_q. \tag{1}$$

With the *d*-axis and the *q*-axis flux linkages defined as:

$$\begin{bmatrix} \psi_d \\ \psi_q \end{bmatrix} = \begin{bmatrix} L_d & 0 \\ 0 & L_q \end{bmatrix} \begin{bmatrix} i_d \\ i_q \end{bmatrix}. \tag{2}$$

The torque model is modified as:

$$T_e = \frac{3}{2}\frac{P}{2}\left(\frac{1}{L_q} - \frac{1}{L_d}\right)\psi_d\psi_q. \tag{3}$$

Both self and mutual inductances have been reported in [24] as functions of the currents i_d and i_q in a cross-saturated PMSM. Flux linkage relationship considering cross-saturation is, therefore, shown in equation (4).

$$\begin{bmatrix} \psi_d \\ \psi_q \end{bmatrix} = \begin{bmatrix} L_d(i_d,i_q) & M_{dq}(i_d,i_q) \\ M_{qd}(i_d,i_q) & L_q(i_d,i_q) \end{bmatrix} \begin{bmatrix} i_d \\ i_q \end{bmatrix}. \tag{4}$$

Although $M_{dq}(i_d,i_q)$ and $M_{qd}(i_d,i_q)$ are equal, it is very complex to identify and separate the self and mutual inductance terms experimentally. Therefore, a simplified approach is used which defines the *d* and *q*-axis currents as quotients of flux linkages and inductances thus $i_d = \psi_d/L_d(i_d,i_q)$

and $i_q = \psi_q / L_q(i_d, i_q)$. Using this assumption, the mutual inductances in equation (4) are modelled within the self-inductances as shown in equation (5).

$$\left[\begin{array}{c} \psi_d \\ \psi_q \end{array} \right] = \left[\begin{array}{cc} L_d(i_d, i_q) & 0 \\ 0 & L_q(i_d, i_q) \end{array} \right] \left[\begin{array}{c} i_d \\ i_q \end{array} \right]. \tag{5}$$

From this modification, equation (3) is rewritten with the inductances as functions of the flux linkages as:

$$T_e = \frac{3}{2} \frac{P}{2} \left(\frac{1}{L_q(\psi_d, \psi_q)} - \frac{1}{L_d(\psi_d, \psi_q)} \right) \psi_d \psi_q. \tag{6}$$

Equation (6) clearly presents a conceptual cross-saturated torque model where inductances depend on the flux linkages which in turn depend on the currents thereby making the torque model entirely flux linkage-dependent.

3. Development of a new cross-saturated torque model of the SynRM

With reference to equation (6), a new approach is adopted to develop a flux linkage-based torque model of the SynRM permitting a direct incorporation of cross-saturation effect with reduced computational requirement. The merit of the developed model is that it eliminates the need for look-up tables. To develop the model, a standstill test was conducted on a 5.5 kW SynRM to obtain the flux linkage variation with current for both q and d-axis under saturation and cross-saturation conditions as described in [25–26]. This is a current decay open winding standstill approach that measures $L_d(i_d, i_q)$ and $L_q(i_d, i_q)$ from where $\psi_d(i_d, i_q)$ and $\psi_q(i_d, i_q)$ are respectively calculated. The schematic is shown in Fig. 1.
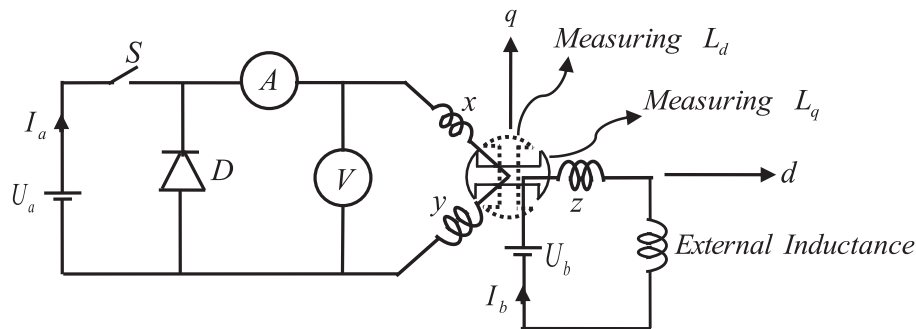

Fig. 1. Schematic of current decay test using open winding fixed rotor method

The synchronous reluctance machine can be described, in the $d-q$ reference frame, by the following set of equations:

$$v_q = R_s i_q + L_q \frac{\mathrm{d} i_q}{\mathrm{d} t} + \omega_r L_d i_d, \tag{7}$$

$$v_d = R_s i_d + L_d \frac{\mathrm{d} i_d}{\mathrm{d} t} - \omega_r L_q i_q. \tag{8}$$

Incorporation of cross-saturation effects with the rotor firmly held at standstill ($\omega_r = 0$) leads to:

$$v_q = R_s i_q + \underbrace{\left(L_q + i_q \frac{\partial L_q}{\partial i_q} \right)}_{L_{qt}} \frac{\mathrm{d}\, i_q}{\mathrm{d}t} + \underbrace{\left(\frac{\partial L_q}{\partial i_d} i_q \right)}_{M_{qd}} \frac{\mathrm{d}\, i_d}{\mathrm{d}t}, \tag{9}$$

$$v_d = R_s i_d + \underbrace{\left(L_d + i_d \frac{\partial L_d}{\partial i_d} \right)}_{L_{dt}} \frac{\mathrm{d}\, i_d}{\mathrm{d}t} + \underbrace{\left(\frac{\partial L_d}{\partial i_q} i_d \right)}_{M_{dq}} \frac{\mathrm{d}\, i_q}{\mathrm{d}t}, \tag{10}$$

where: (L_q, L_d), (L_{qt}, L_{dt}), and (M_{qd}, M_{dq}) are the apparent, transient and mutual inductances respectively.

The switch S can be switched off to obtain current decay through the diode D. Current I_a is decayed from a high value of 36A to zero. The rotor is fixed in such a way that I_a represents i_q or i_d in the axis to be measured. The given instant depicted in schematic of Fig. 1 shows that L_q is being measured and I_a is i_q. Cross saturation is introduced by injecting a constant current I_b (0A and 36A) orthogonal to I_a. In the given instant shown in Fig. 1, I_b is i_d. With the procedure described above, $L_d(i_d, i_q)$ and $L_q(i_d, i_q)$ are obtained from where $\psi_d(i_d, i_q)$ and $\psi_q(i_d, i_q)$ are calculated.

The d-q axes flux linkages ψ_d and ψ_q are represented as psi$d$ and psi$q$ respectively. Curve-fitting procedures were done to obtain the best analytical expressions from the experimentally measured flux linkages (both for saturation and cross-saturation conditions) as shown in Figs. 2(a) and 2(b) for the d-axis and q-axis, respectively.

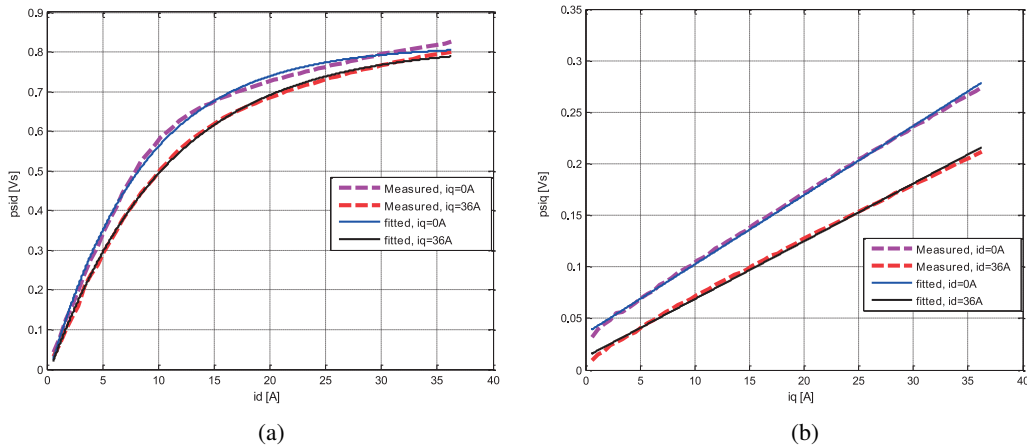(a)   (b)

Fig. 2. Flux linkage against current (measured and curve-fitted): psi$d$ (a); psi$q$ (b)

Fig. 2(a) shows good agreement between the analytical model and the experimentally measured d-axis flux linkage ψ_d for the saturated ($i_q = 0$) and the cross-saturated ($i_q = 36A$) cases. While the Fig. 2(b) shows good agreement between the analytical model and experimentally

measured q-axis flux linkage ψ_q for the saturated ($i_d = 0$) and the cross-saturated ($i_d = 36A$) cases.

The measured d-axis flux linkage ψ_d is curve-fitted and approximated to an exponential function of the form:

$$\psi_d = ae^{-bi_d} + c\,. \tag{11}$$

Similarly, the measured q-axis flux linkage ψ_q is approximated to a linear function of the form:

$$\psi_q = di_q + e\,. \tag{12}$$

The curve-fitting parameters for ψ_d and ψ_q for both saturation and cross-saturation conditions are shown in Table 1.

Table 1. Curve-fitting parameters for flux linkages

Parameters for ψ_d			
$i_q = 0A$ (Saturation)		$i_q = 36A$ (Cross-saturation)	
a_{0A}	-0.8473	a_{36A}	-0.8471
b_{0A}	0.1201	b_{36A}	0.09559
c_{0A}	0.8154	c_{36A}	0.8153
Parameters for ψ_q			
$i_d = 0A$ (Saturation)		$i_d = 36A$ (Cross-saturation)	
d_{0A}	0.006714	d_{36A}	0.00561
e_{0A}	0.03496	e_{36A}	0.01238

For the ψ_d, significant variation in the b parameter is linearized between the two points to obtain the variation of b with i_q as:

$$b = m_1 i_q + k_1\,, \tag{13}$$

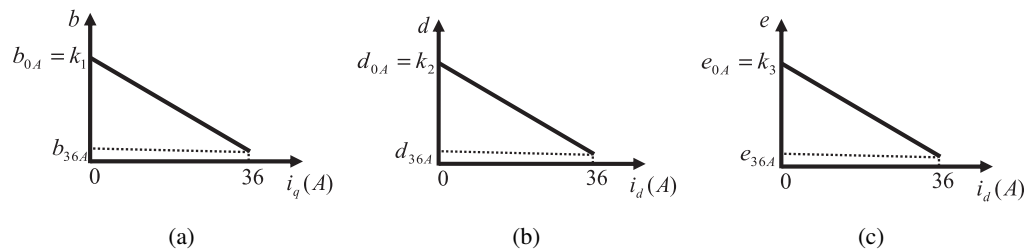where: m_1 is the slope of Fig. 3(a) and k_1 is the initial value of b at $i_q = 0$.

Fig. 3. Parameter linearization plots

Substituting equation (13) into equation (11) gives:

$$\psi_d = ae^{-(m_1 i_q + k_1)i_d} + c\,. \tag{14}$$

For ψ_q, the variations in the d and e with respect to i_d are linearized to obtain:

$$d = m_2 i_d + k_2\,, \tag{15}$$

$$e = m_3 i_d + k_3\,, \tag{16}$$

where: m_2 and m_3 are the slopes of Fig. 3(b) and Fig. 3(c) respectively while k_2 and k_3 are their respective intersections (initial values) at $i_d = 0$.

Substituting equation (15) and equation (16) into equation (12) gives equation (17) as:

$$\psi_q = m_2 i_d i_q + k_2 i_q + m_3 i_d + k_3\,. \tag{17}$$

Equation (14) and equation (17) are the cross-saturated flux linkages for the SynRM while the parameters a, c, m_1, m_2, m_3, k_1, k_2, k_3 are curve fitting parameters that vary with the accuracy of the curve-fitting.

Fig. 4 (a and b) and Fig. 5(a and b) show the agreement in 3D for the proposed analytical stator flux linkage models of equation (14) and equation (17) respectively with the experimentally measured flux linkages obtained using the test bench schematic and set-up of Fig. 6 and Fig. 7 as described in [27–28]. It consists of a 5.5 kW SynRM test machine controlled with a dSpace MicroLabBox Kintex 7 at a switching frequency of 10 kHz. The parameters of the experimental SynRM are shown in the Table 2. The flux linkages, $\psi_d(i_d, i_q)$ and $\psi_q(i_d, i_q)$ are recorded using the oscilloscope function of the dSpace Control Desk 5.4. Current is measured with LEM current sensors while torque is measured at the shaft with a Magtrol torque transducer.
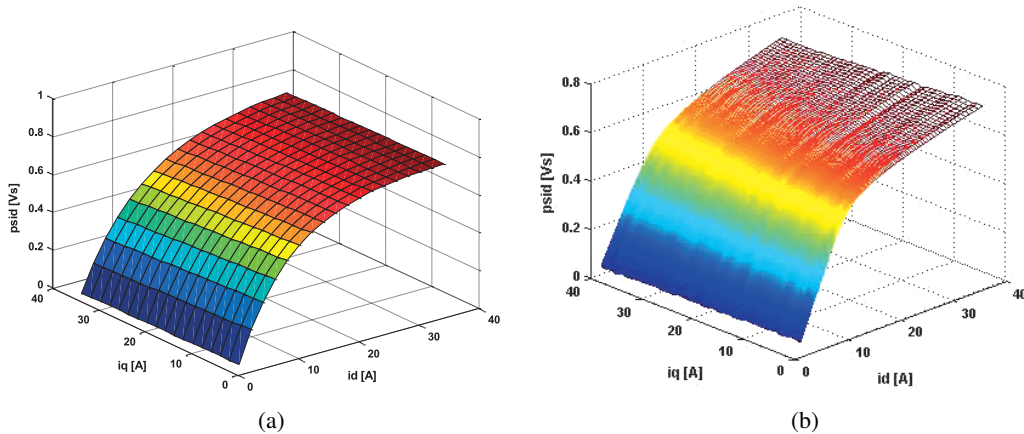

(a)   (b)

Fig. 4. Cross-saturated *d*-axis stator flux linkage psi *d*: analytical (a); measured (b)

The cross-saturated flux linkage-based torque model is obtained by reversing equations (14) and (17) to obtain $i_d(\psi_d, \psi_q)$ and $i_q(\psi_d, \psi_q)$ respectively. The procedure is as follows:

From equation (14),

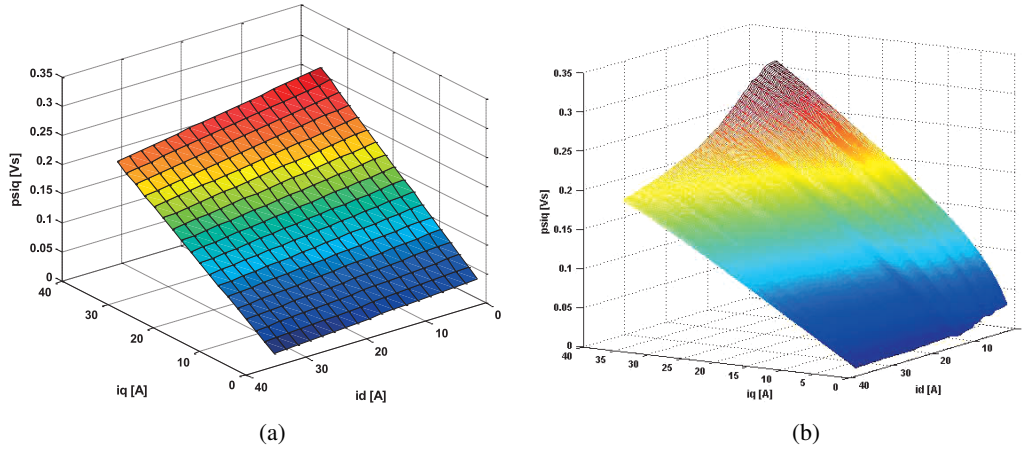$$i_q = \frac{\ln\left(\dfrac{\psi_d - c}{a}\right) + k_1 i_d}{-m_1 i_d}\,. \tag{18}$$

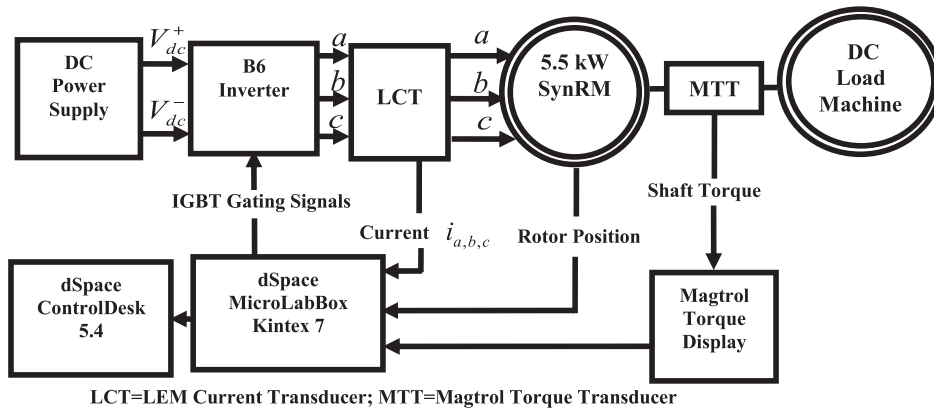Fig. 5. Cross-saturated *q*-axis stator flux linkage psi *q*: analytical (a); measured (b)

LCT=LEM Current Transducer; MTT=Magtrol Torque Transducer

Fig. 6. Test bench schematic
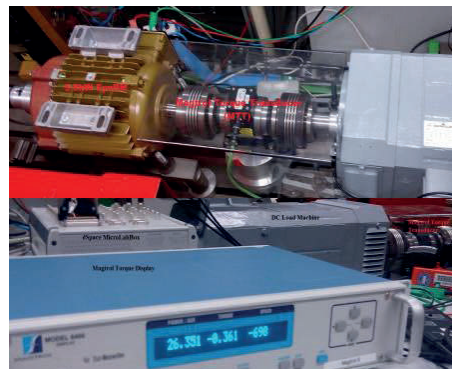
Fig. 7. Test bench set-up

Table 2. Parameters of the experimental SynRM

1	Rated power, kW	5.5
2	Rated voltage, V	220
3	Rated torque, Nm	17.5
4	Rated speed, rpm	3000
5	Stator resistance (20°C), Ω	0.357
6	Moment of inertia, Kgm^2	0.019
7	No. of poles (P)	4

Substituting equation (18) into equation (17) and rearranging;

$$\left[\frac{m_2 k_1}{m_1} - m_3\right] i_d^2 + \left[\psi_q + \frac{m_2}{m_1} \ln\left(\frac{\psi_d - c}{a}\right) + \frac{k_2 k_1}{m_1} - k_3\right] i_d + \frac{k_2}{m_1} \ln\left(\frac{\psi_d - c}{a}\right) = 0. \quad (19)$$

The following definitions are made from equation (19):

$$\sigma_4 = \ln\left(\frac{\psi_d - c}{a}\right), \quad (20)$$

$$\sigma_3 = \frac{m_2 k_1}{m_1} - m_3, \quad (21)$$

$$\sigma_2 = \psi_q + \frac{m_2}{m_1} \sigma_4 + \frac{k_2 k_1}{m_1} - k_3. \quad (22)$$

Equation (19) modifies to

$$\sigma_3 i_d^2 + \sigma_2 i_d + \frac{k_2}{m_1} \sigma_4 = 0. \quad (23)$$

Equation (23), being quadratic, is solved resulting in two expressions for i_d:

$$i_d+ = \frac{-\sigma_2 + \sigma_1}{2\sigma_3} \quad (24)$$

and

$$i_d- = \frac{-\sigma_2 - \sigma_1}{2\sigma_3}, \quad (25)$$

where

$$\sigma_1 = \sqrt{\sigma_2^2 - \frac{4\sigma_3 \sigma_4 k_2}{m_1}}. \quad (26)$$

i_d+ and i_d- are plotted against q-axis and d-axis flux linkages (ψ_q and ψ_d). The plot of i_d+ is found to be out of range while the plot of i_d- is within and is shown in Fig. 8(a). i_d- is adopted as the solution for i_d.
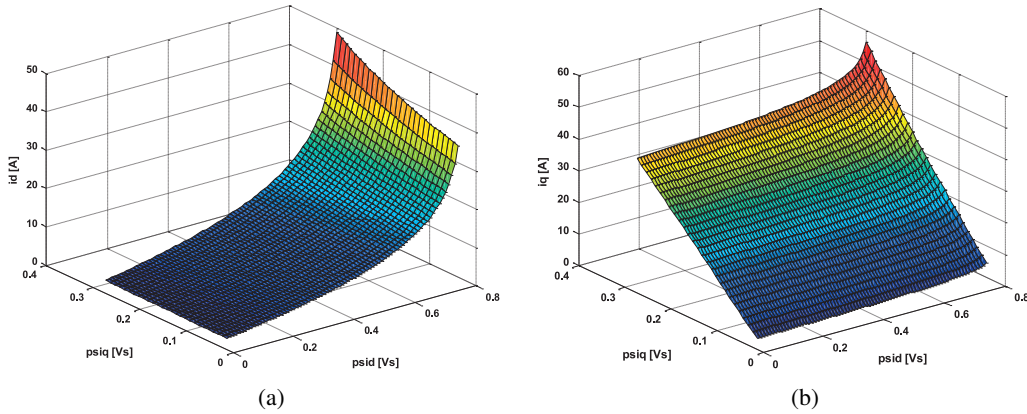
Fig. 8. Analytical stator current as a function of flux Linkages: d-axis stator current i_d (a); q-axis stator current i_q (b)

Substituting equation (25) into equation (18) and simplifying gives:

$$i_q = \frac{2\sigma_3\sigma_4 + k_1(-\sigma_2 - \sigma_1)}{-m_1(-\sigma_2 - \sigma_1)}. \tag{27}$$

Equation (27) is plotted and found to be within range as shown in Fig. 8(b).

The current functions are then divided by ψ_d and ψ_q to obtain the respective inductance inverses as:

$$\frac{1}{L_d} = \frac{i_d}{\psi_d} = \frac{-\sigma_2 - \sigma_1}{2\psi_d\sigma_3}, \tag{28}$$

$$\frac{1}{L_q} = \frac{i_q}{\psi_q} = \frac{2\sigma_3\sigma_4 + k_1(-\sigma_2 - \sigma_1)}{-m_1\psi_q(-\sigma_2 - \sigma_1)}. \tag{29}$$

Introducing the cross-saturated inductance inverses into equation (6) results in the cross-saturated torque model of equation (30).

$$T = \frac{3}{2}\frac{P}{2}\psi_d\psi_q \left(\frac{2\sigma_3\sigma_4 - k_1(\sigma_2 + \sigma_1)}{m_1\psi_q(\sigma_2 + \sigma_1)} + \frac{\sigma_2 + \sigma_1}{2\psi_d\sigma_3} \right). \tag{30}$$

Equation (30) is a cross-saturated torque model of the SynRM with direct incorporation of nonlinear cross-saturation effects. The developed model demonstrates reduced computational effort since $a = -0.8473$, $c = 0.8154$, $k_1 = 0.1201$, $k_2 = 0.0067$, $k_3 = 0.0350$, $m_1 = -6.7639 \times 10^{-4}$, $m_2 = -3.0467 \times 10^{-5}$ and $m_3 = -6.2313 \times 10^{-4}$ are parameters arising from the curve fitting curve. Mainly, one additional logarithm and one square root function has to be considered and this poses no computational challenge to modern processors.

Finally, equation (30) is plotted for comparison with the experimental torque data as shown in Fig. 9 and very close conformity is observed thereby validating the developed model. The observed torque difference, primarily due to the effect of iron and friction losses, is analysed in the next section.
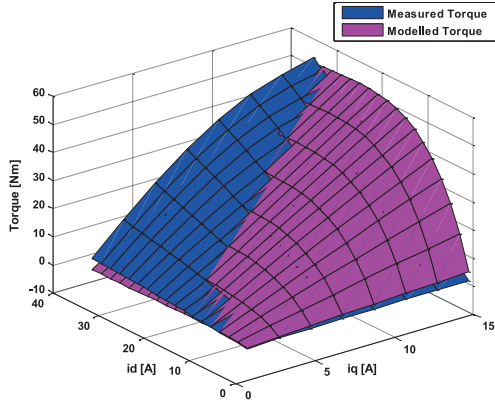
Fig. 9. Torque against *d*-axis and *q*-axis currents

4. Comparison of the experimental results and the developed model

Since the cross-saturated torque model of equation (30) does not incorporate the effects of friction and iron losses, the measured mechanical shaft torque is compared with the analytical cross-saturated torque model by subtracting the effects of friction and iron losses. Iron losses are identified by calculating copper losses considering measured temperature and subtracting from total machine losses. The torque error between the measured mechanical shaft torque and modelled analytical cross-saturated torque model is calculated with equation (31).

$$\Delta T = T_{\mathrm{es}} - T_{\mathrm{meas}} - T_{\mathrm{friction}} - \frac{P_{\mathrm{iron}}}{\omega_{\mathrm{mech}}} \,. \tag{31}$$

The results of comparison of estimated and measured (experimental) torque, where a loss optimal flux is calculated and commanded at each operating point, are shown in Fig. 10(a) and Fig. 10(b). Loss optimal flux-linkage is determined using the Lagrange Function as described in [26]. Since optimal flux-linkage minimizes losses, flux-linkage based machine losses (copper losses, hysteresis losses and eddy current losses) and inverter losses (conduction losses and switching losses) are formulated and minimized to obtain loss optimal flux linkage for the demanded torque considering voltage and current limits as inequality constraints. Torque error indicates the deviation between estimated and measured (experimental) torque (in Nm and %) which represents friction losses and torque difference caused by iron losses which have been subtracted from estimated torque T_{es}.

As can be seen from the 3D plot of Fig. 10(a), a maximum torque error of 0.6 Nm is obtained for the measured operating points but since the loss optimal flux for the commanded operating points for different speeds of operation are not exactly the same, percentage (%) torque error is most appropriate for graphical comparison.

As seen in Fig. 10(b), the percentage (%) torque error decreases with increase in commanded loss optimal flux for each of the operating speeds. In other words, the higher the operating point current and loss optimal flux command, the lower the percentage torque error. This confirms that the iron losses are more at the lower current/flux regime.
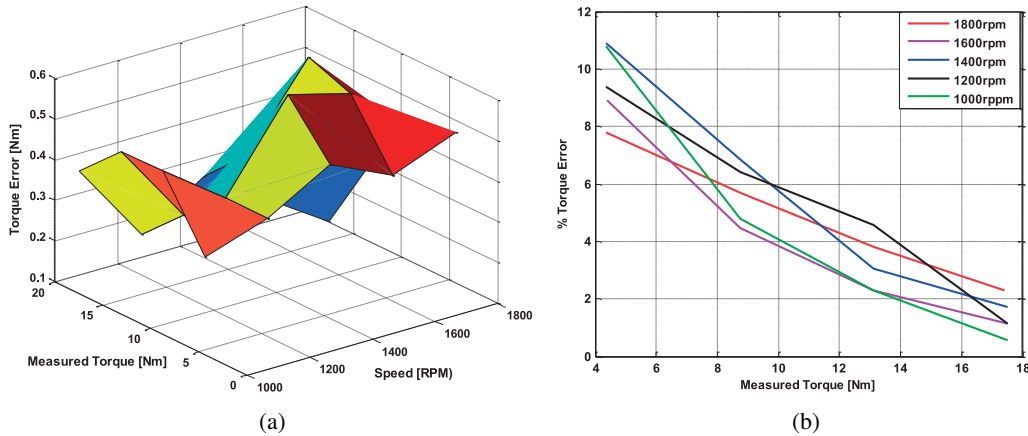
Fig. 10. Torque error and % torque error: torque error (a); % torque error (b)

5. Conclusions

This paper has presented a new torque model of the synchronous reluctance machine (SynRM) including a direct incorporation of cross-saturation effects without the use of look-up tables. Experimentally measured flux linkages for both saturation and cross saturation conditions were curve-fitted and linearized to obtain approximate expressions for both the *d*-axis and *q*-axis flux linkages. These are subsequently employed in the conceptual torque equation to obtain the new saturated torque model as a function of the flux linkages. The developed model demonstrates reduced computational effort, essentially incorporating one additional logarithm and square root function which do not pose computational challenge to modern microprocessors.

A comparison of the analytical torque and the experimental torque results show close conformity thereby validating the analytical model. Just like in the measured results, the percentage torque error decreases with increase in loss optimal flux command and operating point current. The torque error difference is primarily due to the effect of the unavoidable iron and friction losses.

A typical application is in the deadbeat direct torque and flux control (DB-DTFC) which has emerged as superior alternative to the current vector control (CVC) which, presently, is popularly applied in advanced AC drives. This is the next phase of the research.

References

[1] Ferrari M., Bianchi N., Doria A., Fornasiero E., *Design of synchronous reluctance motor for hybrid electric vehicles*, IEEE Transactions on Industrial Application, vol. 51, no. 4, pp. 3030–3040 (2015).

[2] Ikaheimo J., Kolehmainen J., Kansakangas T., Kivela V., Moghaddam R., *Synchronous high-speed reluctance machine with novel rotor construction*, IEEE Transactions on Industrial Electronics, vol. 61, no. 6, pp. 2969–2975 (2014).

[3] Baek J., Bonthu S., Kwak S., Choi S., *Optimal design of five phase permanent magnet assisted synchronous reluctance motor for low output torque ripple*, Proceedings of the IEEE Energy Conversion & Expo (ECCE), Pittsburgh, USA, CD-ROM (2014).

[4] Zhang X., Foo G., Vilathgamuwa D., Maskell D., *An improved robust field-weakening algorithm for direct-torque-controlled synchronous-reluctance-motor drives*, IEEE Transactions on Industrial Electronics, vol. 62, no. 4, pp. 3255–3264 (2015).

[5] Qu Z., Tuovinen T., Hinkkanen M., *Inclusion of magnetic saturation in dynamic models of synchronous reluctance motors*, Proceedings of the 20th International Conference on Electrical Machines (ICEM), Marseille, France, pp. 994–1000 (2012).

[6] Foo G., Zhang X., *Robust direct torque control of synchronous reluctance motor drives in the field-weakening region*, IEEE Transactions on Power Electronics, vol. 32, no. 3, pp. 1289–1298 (2017).

[7] Foo G., Zhang X., *Robust constant switching frequency-based field-weakening algorithm for direct torque controlled reluctance synchronous motors*, IEEE Transactions on Industrial Informatics, vol. 12, no. 4, pp. 1462–1473 (2016).

[8] Ferdous S., Garcia P., Oninda M., Hoque M., *MTPA and field weakening control of synchronous reluctance motor*, Proceedings of the 9th International Conference on Electrical and Computer Engineering (ICECE), Dhaka, Bangladesh, pp. 598–601 (2016).

[9] Chui M., Chiang J., Lee J., Gaing Z., *Multi-objective optimization design of interior permanent-magnet synchronous motors for improving the effectiveness of field weakening control*, Proceedings of the 17th International Conference on Electrical Machines and Systems (ICEMS), Hangzhou, China, pp. 517–521 (2014).

[10] Mingardi D., Morandin M., Bolognani S., Bianchi N., *On the proprieties of the differential cross-saturation inductance in synchronous machines*, IEEE Transactions on Industrial Application, vol. 53, no. 2. pp. 991–1000 (2016).

[11] Huang W., Zhang Y., Zhang X., Sun G., *Accurate torque control of interior permanent magnet synchronous machine*, IEEE Transactions on Energy Conversion, vol. 29, no. 1, pp. 29–37 (2014).

[12] Morales-Caporal R., Pacas M., *Impact of the magnetic cross-saturation in a sensorless direct torque controlled synchronous reluctance machine based on test voltage signal injections*, Proceedings of the 34th Annual Conference of IEEE Industrial Electronics (IECON 2008), Orlando Florida, USA, pp. 1234–1239 (2008).

[13] Armando E., Bojoi R., Guglielmi P., Pellegrino G., Pastorelli M., *Experimental identification of the magnetic model of synchronous machines*, IEEE Transactions on Industrial Application, vol. 49, no. 5, pp. 2116–2125 (2013).

[14] Rahman H., Hiti S., *Identification of machine parameters of a synchronous motor*, IEEE Transactions on Industrial Application, vol. 41, no. 2, pp. 557–565 (2005).

[15] Niazi P., Toliyat H., *Online parameter estimation of permanent-magnet assisted synchronous reluctance motor*, IEEE Transactions on Industrial Application, vol. 43, no. 2, pp. 609–615 (2007).

[16] Noguchi T., Kumakiri Y., *On-line parameter identification of IPM motor using instantaneous reactive power for robust maximum torque per ampere control*, Proceedings of the IEEE International Conference on Industrial Technology (ICIT), Seville, Spain, pp. 793–799 (2015).

[17] Ichikawa S., Tomita M., Doki S., Okuma S., *Sensorless control of synchronous reluctance motors based on extended emf models considering magnetic saturation with online parameter identification*, IEEE Transactions on Industrial Application, vol. 42, no. 5, pp. 1264–1274 (2006).

[18] Senjyu T., Kinjo K., Urasaki N., Uezato K., *High efficiency control of synchronous reluctance motors using extended Kalman filter*, IEEE Transactions on Industrial Electronics, vol. 50, no. 2, pp. 726–732 (2003).

[19] Kock H., Rix A., Kamper M., *Optimal torque control of synchronous machines based on finite-element analysis*, IEEE Transactions on Industrial Electronics, vol. 57, no. 1, pp. 413–419 (2010).

[20] Tahi S., Ibtiouen R., *Finite element calculation of the dq-axes inductances and torque of synchronous reluctance motor*, Proceedings of the IEEE International Conference on Electrical Sciences and Technologies in Maghreb (CISTEM), Tunis, Tunisia, pp. 1–5 (2014).

[21] Boroujeni S., Bianchi N., Alberti L., *Fast estimation of line-start reluctance machine parameters by finite element analysis*, IEEE Transactions on Energy Conversion, vol. 26, no. 1, pp. 1–8 (2011).

[22] Ogbuka C., Nwosu C., Agu M., *Dynamic and steady state performance comparison of line-start permanent magnet synchronous motors with interior and surface rotor magnets*, Archives of Electrical Engineering, vol. 65, no. 1, pp. 105–116 (2016).

[23] Pillay P., Krishnan R., *Modeling, simulation, and analysis of permanent magnet motor drives I: the permanent magnet synchronous motor drive*, IEEE Transaction on Industrial application, vol. 25, pp. 265–273 (1989).

[24] Kellner S., Piepenbreier B., *General PMSM d,q-model using optimized interpolated absolute and differential inductance surface*, Proceedings of the IEEE International Electric Machines & Drives Conference (IEMDC 2011), Ontorio, Canada, pp. 212–217 (2011).

[25] Kilthau A., Pacas J., *Parameter-measurement and control of the synchronous reluctance machine including cross saturation*, Proceedings of the IEEE Thirty-Sixth IAS Annual Meeting Conference of the Industry Applications Society, Chicago, IL, USA, pp. 2302–2309 (2001).

[26] Saur M., Lehner B., Hentschel F., Gerling D., Lorenz R., *DB-DTFC as loss minimizing control for synchronous reluctance drives*, Proceedings of IEEE 41st Annual Conference of the Industrial Electronics Society (IECON 2015), Yokohama, Japan, pp. 1412–1417 (2015).

[27] Stumberger B., Stumberger G., Dolinar D., Hamler A., Trlep M., *Evaluation of saturation and cross-magnetization effects in interior permanent-magnet synchronous motor*, IEEE Transactions on Industrial Application, vol. 39, no. 5, pp. 1264–1271 (2003).

[28] Saur M., Ramos F., Perez A., Gerling D., Lorenz R.D., *Implementation of deadbeat-direct torque and flux control for synchronous reluctance machines to minimize loss each switching period*, Proceedings of the IEEE Applied Power Electronics Conference and Exposition (APEC), Long Beach, CA, USA, pp. 215–220 (2016).